Supporting Information

Role of topological surface states and mirror symmetry in topological crystalline insulator SnTe as an efficient electrocatalyst

Qing Qu[1, 3†], Bin Liu[2†], Hongtao Liu[2], Jing Liang[2,3], Jiannong Wang[2,3], Ding Pan[2,4] and Iam Keong Sou[1,2,3*]*

[1]Nano Science and Technology Program, The Hong Kong University of Science and Technology, Hong Kong, China.

[2]Department of Physics, The Hong Kong University of Science and Technology, Clear Water Bay, Hong Kong, China.

[3]William Mong Institute of Nano Science and Technology, The Hong Kong University of Science and Technology, Hong Kong, China

[4]Department of Chemistry, The Hong Kong University of Science and Technology, Hong Kong, China.

† These authors contributed equally to this work.
* Corresponding authors

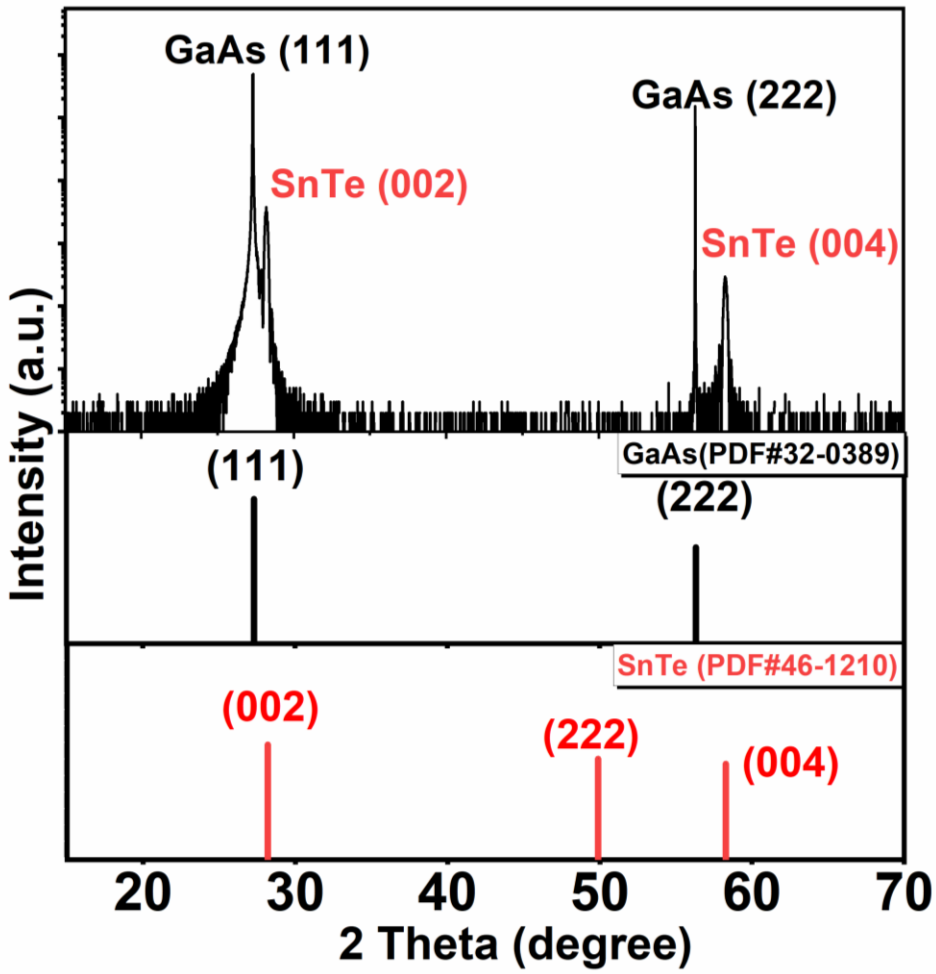

Figure S1. High resolution X-ray diffraction 2θ-ω scan of a SnTe thin film layer directly deposited on a GaAs (111) substrate. The lower part shows the powder diffraction files (PDFs) of SnTe and GaAs as references.

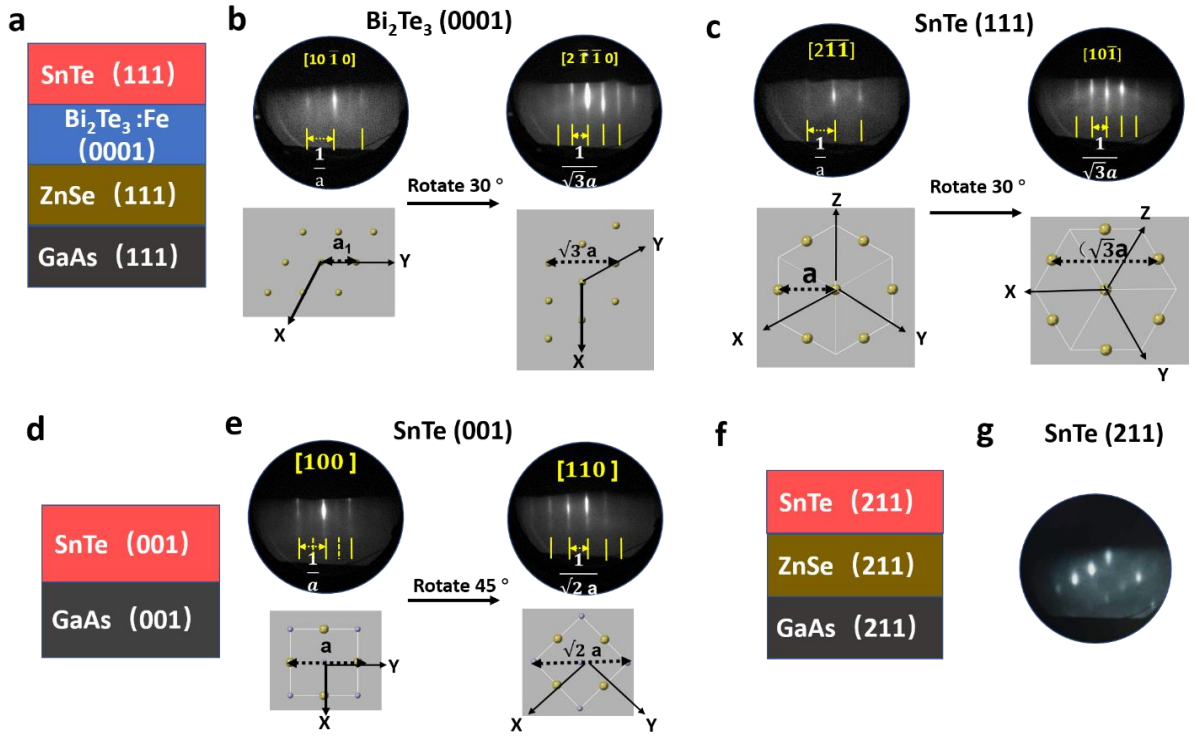

Figure S2. Sample structures and reflection high-energy electron diffraction (RHEED) studies of the three SnTe samples. (a-c) Sample structure and RHEED patterns of Bi_2Te_3 (0001) taken when the electron beam is along the $[10\bar{1}0]$ and $[2\bar{1}\bar{1}0]$ direction and SnTe (111) taken when the electron beam is along the $[2\bar{1}\bar{1}]$ and $[10\bar{1}]$ direction of the SnTe (111) sample. (d, e) Sample structure and RHEED patterns of SnTe (001) taken when the electron beam is along the [100] and [110] direction of the SnTe (001) sample. (f, g) Sample structure and RHEED pattern of SnTe (211) taken when the electron beam is along the $[01\bar{1}]$ direction of the SnTe (211) sample. Schematic drawings at the bottom parts of (b, c, e) are the top views of the respective surface lattices, where the electron beam is oriented directly upward in the page.

Remarks of Figure S2:

Figure S2a displays the sample structure of the SnTe (111) sample. Figures S2b, c exhibit the RHEED patterns of the Bi_2Te_3: Fe (0001) layer and the top SnTe (111) layer, respectively, where the 4-index notation is used in RHEED pattern analysis of Bi_2Te_3. Figure S2b displays the streaky RHEED patterns (corresponding to the reciprocal lattice) of hexagonal Bi_2Te_3:Fe (0001) surface when the incident electron beam is along the $[10\bar{1}0]$ (left) and $[2\bar{1}\bar{1}0]$ (right) direction and the spacing ratio of the streaks of the two azimuths is $\frac{1}{\sqrt{3}}$, which is attributed to the $\sqrt{3}$ ratio in the real space lattices shown at the bottom. Figure S2c shows the streaky RHEED patterns of the triangular SnTe (111) surface when the incident electron beam is along the $[2\bar{1}\bar{1}]$ (left) and $[10\bar{1}]$ (right) direction, and the spacing ratio–of the streaks of the two azimuths is also $\frac{1}{\sqrt{3}}$, which is attributed to the $\sqrt{3}$ ratio in the real space lattices shown at the bottom. The sample structure of the SnTe (001) sample is shown in Figure S2d. Figure S2e displays the RHEED pattern of the SnTe layer when the incident electron beam is along the SnTe [100] (left) and [110] (right) azimuth. The dash lines below the RHEED pattern on the

left corresponds to the surface reconstruction streaks. The left and right RHEED patterns together show that the as-grown SnTe (001) surface has a (2 × 1) surface reconstruction. The spacing ratio of the streaks of the two azimuths is $\frac{1}{\sqrt{2}}$, which is attributed to the $\sqrt{2}$ ratio in the real space lattices shown at the bottom. The sample structure of the SnTe (211) sample is shown in Figure S2f. One RHEED pattern of the SnTe (211) surface is shown in Figure S2g.

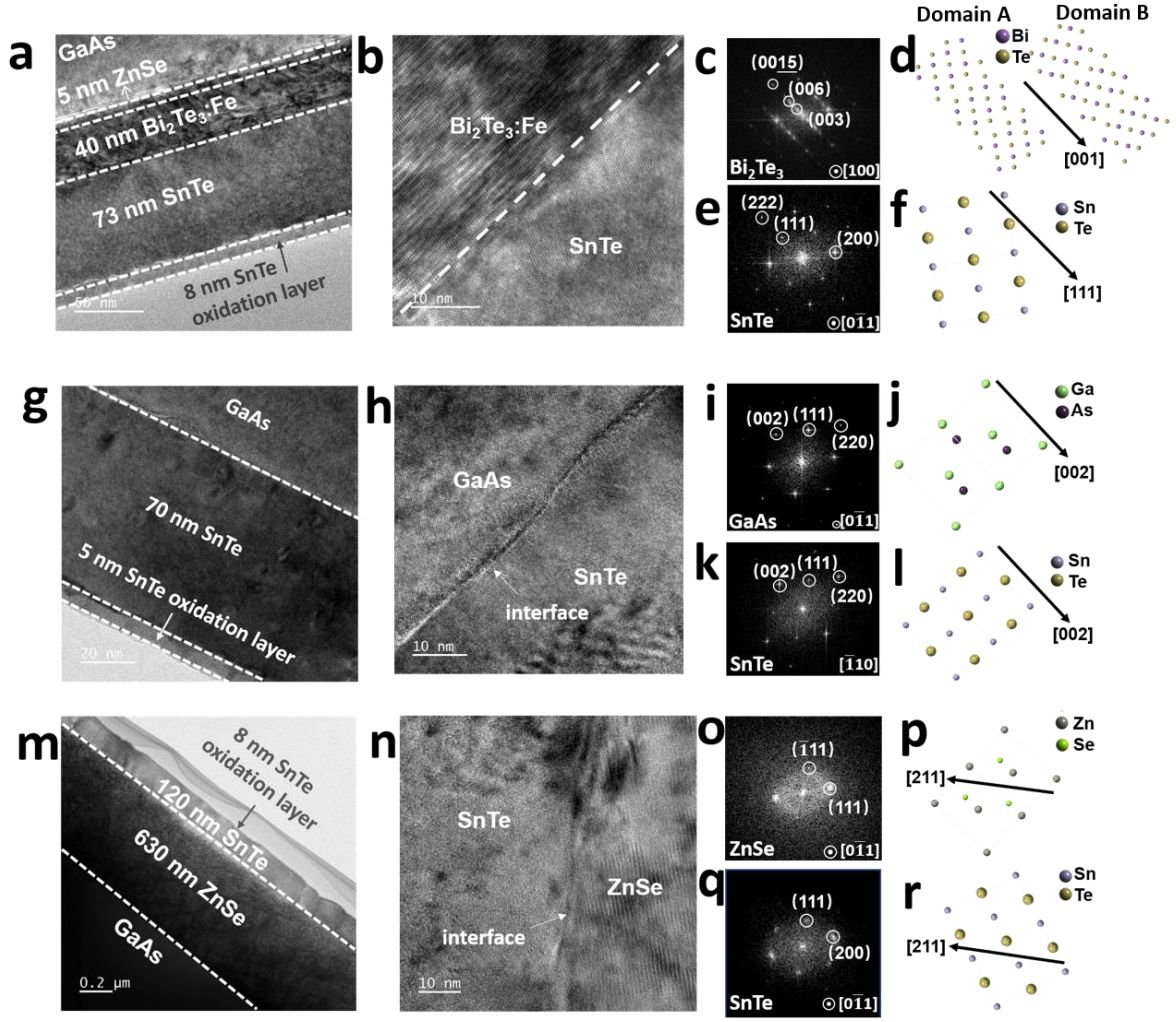

Figure S3. Cross-sectional high-resolution transmission electron microscopy (HRTEM) images and their structural analysis of the three MBE-grown (a-f) SnTe (111), (g-l) SnTe (001), and (m-r) SnTe (211) samples. Cross-sectional high-resolution TEM images of (a-b) SnTe (111), (g-h) SnTe (001) and (m-n) SnTe (211) samples. (c, e, i, k, o, q) The corresponding fast Fourier transform (FFT) patterns of Bi_2Te_3: Fe (001), SnTe (111), GaAs (001), SnTe (001), ZnSe (211) and SnTe (211), respectively. (d, f, j, l, p, r) Schematic drawings of atomic arrangements of Bi_2Te_3:Fe (001), SnTe (111), GaAs (001), SnTe (001), ZnSe (211) and SnTe (211) respectively.

Remarks of Figure S3:

The cross-sectional high-resolution transmission electron microscopy (HRTEM) images with fast Fourier transform (FFT) images and corresponding atomic arrangements of the three SnTe

samples studied in this work are shown in Figure S3. The thicknesses of the different layers of the three samples are determined from the cross-sectional TEM images shown in Figure S3a, g, m. As can be seen, the 73 nm SnTe (111) layer was grown on the 40 nm Bi_2Te_3:Fe (001) layer with a 5 nm ZnSe buffer layer (Figure S3a), the 70 nm SnTe (001) layer was grown on a GaAs (001) substrate directly (Figure S3g), and the 120 nm SnTe (211) layer was grown on the 630 nm (211) ZnSe buffer layer (Figure S3m). It should be noted that one should only take these values as the approximate nominal thicknesses since these samples have domains or the valley structures at their surfaces, which will be addressed later. It should also be mentioned that the cross-sectional TEM images of the three samples show that a thin oxidation layer of 5–8 nm exists at their surfaces, which is believed to be formed mainly via the reaction with the water and the G2 epoxy used during the TEM sample preparation.

The cross-sectional HRTEM image of the interface portion between the Bi_2Te_3: Fe (001) layer and the SnTe (111) layer of the SnTe (111) sample is displayed in Figure S3b. The energy dispersive spectroscopy (EDS) profile shown in Figure S5 indicates that the incorporated Fe concentration is about 0.8% (Table S1), which is close to the value of a similar Bi_2Te_3:Fe layer we reported previously.[1] The FFT pattern of the Bi_2Te_3:Fe (001) layer shown in Figure S3c reveals that two sets of hexagonal lattice appear in this thin film layer, indicating the existence of twin crystals,[1-3] attributed to the fact the (001)-oriented Bi_2Te_3 has a 3-fold symmetry, while the GaAs (111) substrate has a 6-fold symmetry. Figure S3d displays the schematic drawings of the two expected domains of the (001)-oriented Bi_2Te_3. Figure S3e, f display the FFT pattern and its corresponding atomic arrangement of the SnTe (111) layer. The FFT patterns shown in Figure S3c, e indicate the relationship of the $[111]_{SnTe}//[001]_{Bi_2Te_3:Fe}$. Figure S3h, i, k, j, l show the cross-sectional HRTEM image, FFT patterns and the corresponding schematic drawings of the atomic arrangement of the (001)-oriented SnTe layer of the SnTe (001) sample. As shown in Figure S3h, the interface between the SnTe (001) and GaAs (001) lattices as indicated by the arrow is not atomically flat, which is attributed to the outgassing of the GaAs (001) substrate without applying an As over pressure (which is not available in our MBE system) and the large lattice mismatch between SnTe and GaAs. Figure S3n exhibits the cross-sectional HRTEM image of the SnTe (211)/ZnSe (211) interface portion. It can be seen that the interface between the SnTe (211) and ZnSe (211) lattices as indicated by the arrow shows a wavy feature, which is attributed to the step edges of the (211) surface and the large lattice mismatch between SnTe and ZnSe, similar to the cases of the ZnTe/GaAs (211)[4] and ZnTe/Si (211)[5] systems. Figure S3o, p show the FFT pattern and the corresponding drawing of the atomic arrangement (211)-oriented ZnSe, and Figure S3q, r display the FFT pattern and drawing of the (211)-oriented SnTe grown on the (211)-oriented ZnSe. All the three relationships of the $[111]_{SnTe}//[001]_{Bi_2Te_3:Fe}$, $[001]_{SnTe}//[001]_{GaAs}$, $[211]_{SnTe}//[211]_{ZnSe}$ mentioned above are consistent with the HRXRD profiles shown in Figure 1.

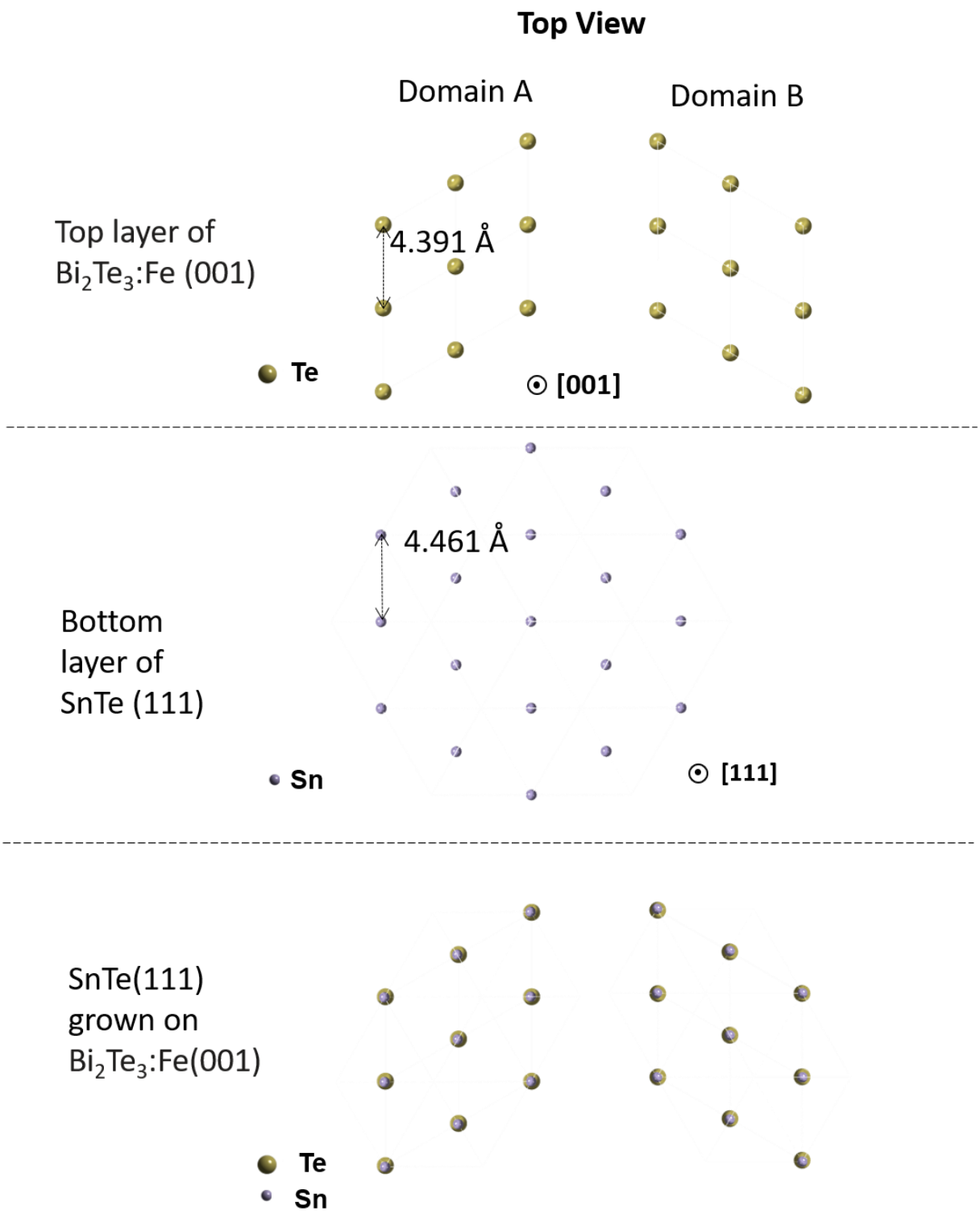

Figure S4. The top-view atomic match correlation between the two domains of Bi_2Te_3:Fe (001) and SnTe (111).

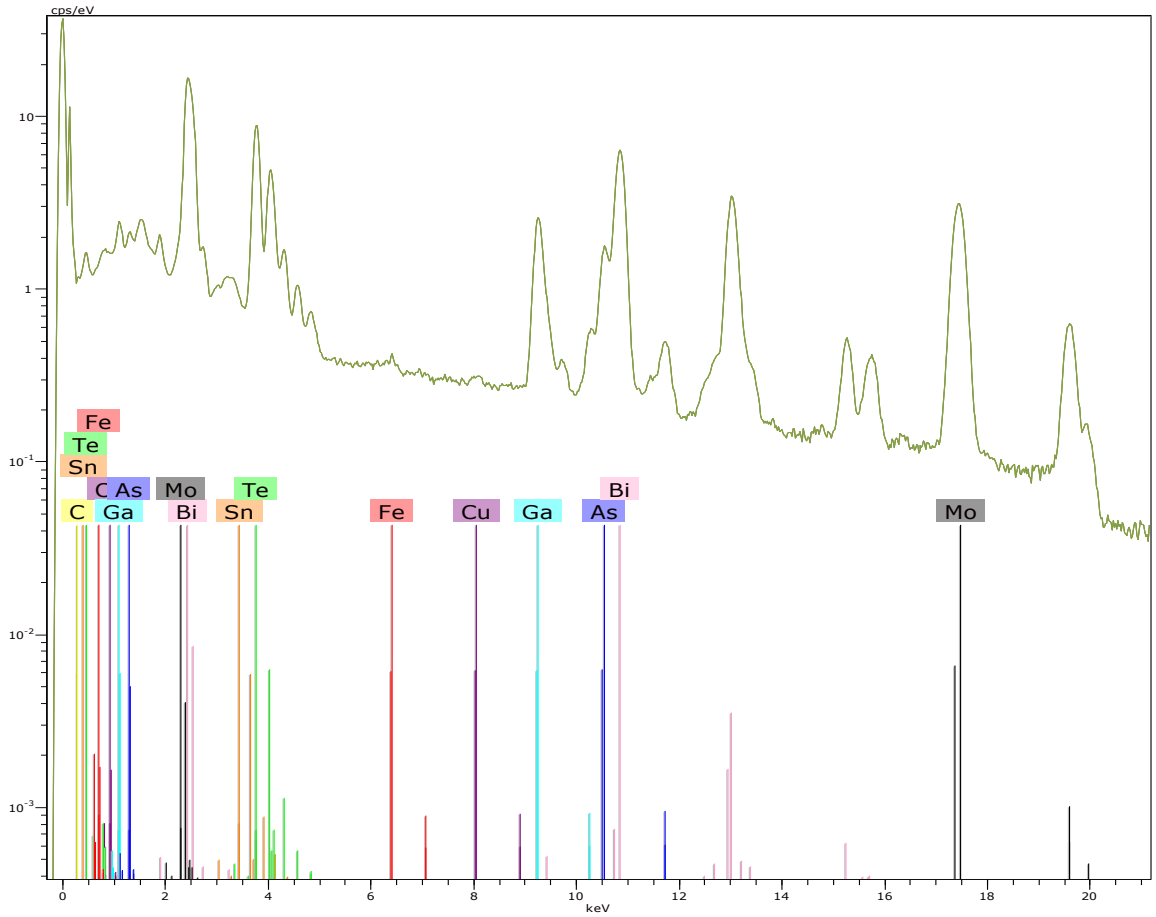

Figure S5. Energy dispersive spectroscopy (EDS) profile of the Bi_2Te_3:Fe layer indicates that the incorporated Fe concentration is about 0.80% (Table S1), where the Mo signal comes from the Mo sample holder used for the EDS measurements and the Cu signal comes from the contamination from the ion-milling chamber for TEM sample preparation as many users used Cu-grid sample holders for this process.

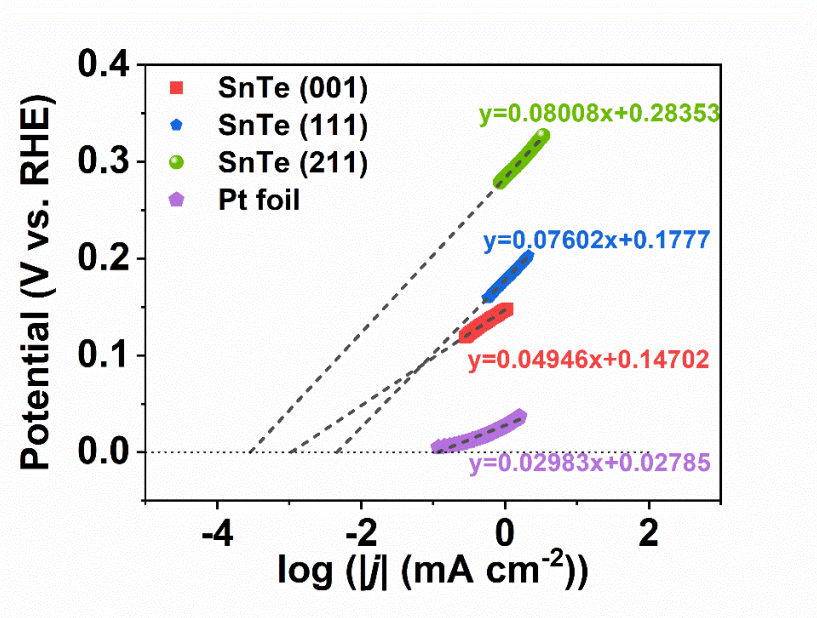

Figure S6. Exchange current densities (j_0) for the active materials in Figure 3a can be derived from the x-intercepts of the fitted dash lines extrapolated from the Tafel plots shown in colors.

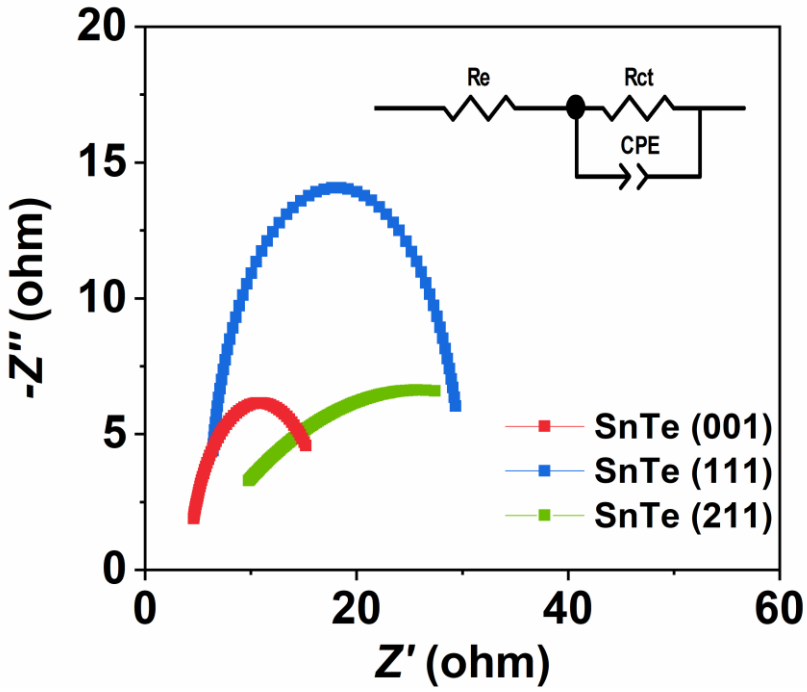

Figure S7. Nyquist plots of the SnTe (001), SnTe (111) and SnTe (211) samples.

Remarks of Figure S7:

Within the period for taking an EIS spectrum, the system being measured must be at a steady state and the potential of such a state is usually determined by finding out the open-circuit

potential (OCP) of the system. OCP is the difference between the potential of the working electrode and that of the reference electrode when the cell is at open-circuit status. In our studies, the determination of the OCP value for a sample lasts for at least one hour. After inserting the sample to the electrolyte, we define the system is under static state if the OCP value changes no more than 1mV within 10 mins. For different samples, the OCP values are different as they depend on parameters like surface inhomogeneity and roughness, thus the EIS measurements are usually conducted at the sample's own OCP value.

Both the Nyquist plots of the SnTe (001) and SnTe (111) samples present typical semicircle profiles, while the Nyquist plot of SnTe (211) shows an arc of a circle with its center lying some distance below the x-axis (in the fourth quadrant). Most of the researchers describe the feature of the Nyquist plots similar to that of SnTe (211) as depressed and/or deformed semicircles [6-9]. A possible cause for such depressed semicircles is attributed to the deviation from a smooth electrode surface [10], causing an uneven current distribution on the electrode due to the surface inhomogeneous and roughness [11-15]. This observation is also consistent with the AFM image analysis shown in Figure 2 that the surface of the SnTe (211) sample exhibits the roughest surface morphology compared with the surfaces of the SnTe (001) and SnTe (111) samples.

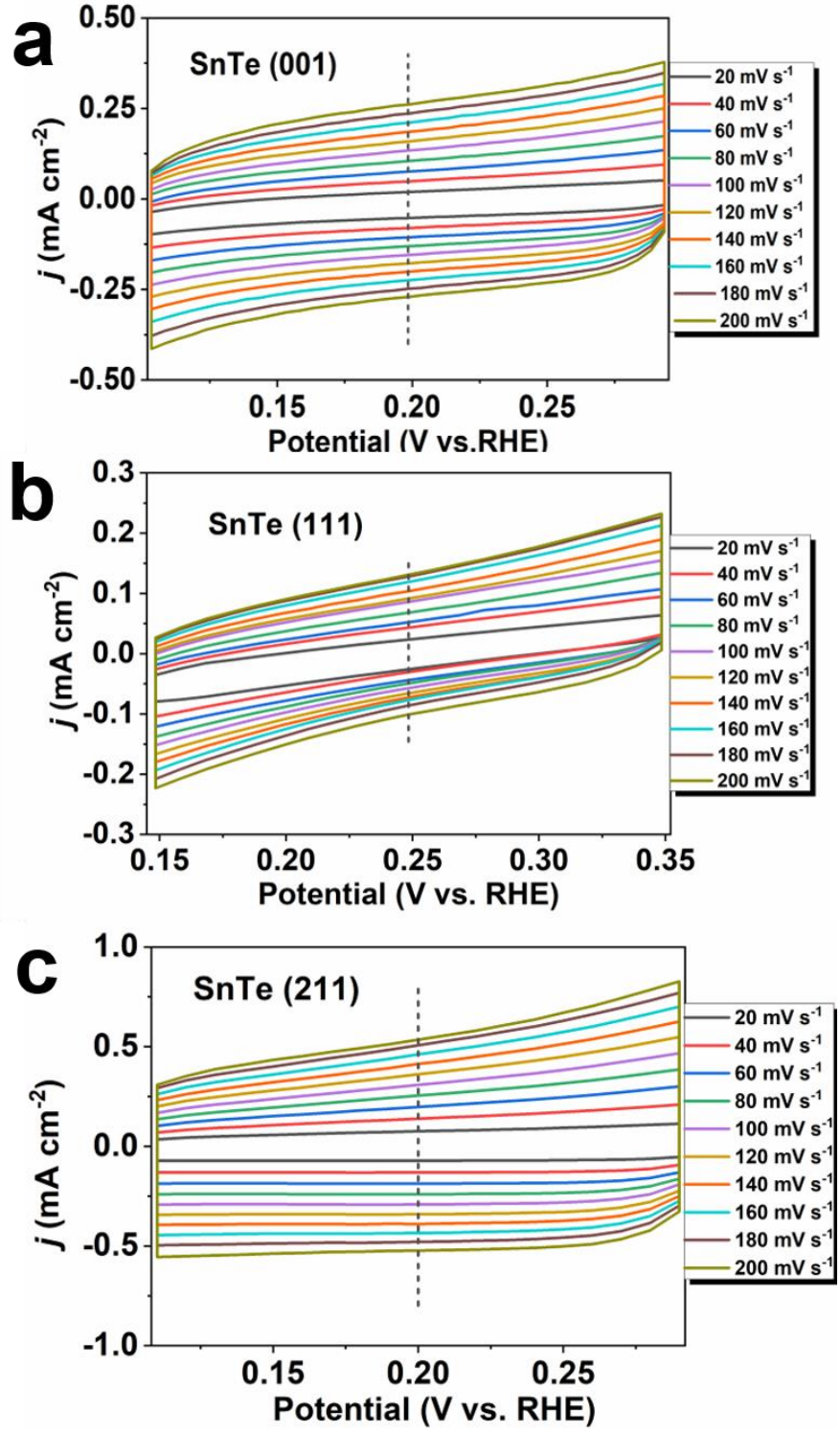

Figure S8. Electrochemical surface area measurements. Cyclic voltammograms (CV) curves with different scan rates of the (a) SnTe (001), (b) SnTe (111) and (c) SnTe (211) samples.

Supplementary note 1

Measurement of the electrochemical specific capacitance

To measure the electrochemical specific capacitance of the SnTe (001), (111) and (211) samples, the potentials were swept at each of ten different scan rates (20, 40, 60, 80, 100, 120, 140, 160, 180 and 200 mV/s).

Figure S8 shows the results of these cyclic voltammetry (CV) measurements. We measured the capacitive currents in the potential ranges of the curves in Figure S8 where no faradic processes are observed, and the capacitive current densities ($(j_{anodic}-j_{cathodic})/2$ taken at the potential values of the dash lines) are plotted as a function of the scan rate as shown in Figure 3c.

Calculation of the electrochemical active surface area

The C_{dl} values can be converted into the electrochemically active surface areas (ECSA) using the specific capacitance value for a flat standard with 1 cm^2 of real surface area. The specific capacitance for a flat surface is generally found to be in the range of 20-60 μF cm^{-2} [16-19]. In the following calculations for obtaining the TOF values, we take 40 μF cm^{-2} as a moderate value, and define the A_{ECSA} as:

$$\mathrm{A_{ECSA}} = \frac{C_{\mathrm{dl}}}{40\ \mu\mathrm{F\ cm^{-2}per\ cm^2_{ECSA}}}$$

Thus the ECSA values of the three SnTe samples can be calculated as shown below.

$$\mathrm{A_{ECSA}^{SnTe\ (001)}} = \frac{1.280\ \mathrm{mF\ cm^{-2}}}{40\ \mu\mathrm{F\ cm^{-2}per\ cm^2_{ECSA}}} = 32\mathrm{cm^2_{ECSA}}$$

$$\mathrm{A_{ECSA}^{SnTe\ (111)}} = \frac{0.503\ \mathrm{mF\ cm^{-2}}}{40\ \mu\mathrm{F\ cm^{-2}per\ cm^2_{ECSA}}} = 12.575\ \mathrm{cm^2_{ECSA}}$$

$$\mathrm{A_{ECSA}^{SnTe\ (211)}} = \frac{2.55\ \mathrm{mF\ cm^{-2}}}{40\ \mu\mathrm{F\ cm^{-2}per\ cm^2_{ECSA}}} = 63.75\mathrm{cm^2_{ECSA}}$$

Turnover frequency calculations

To calculate the per-site turnover frequency (TOF), we used the following formula:

$$\mathrm{TOF} = \frac{\mathrm{number\ of\ total\ hydrogen\ turnover/\ cm^2\ of\ geometric\ area}}{\mathrm{number\ of\ active\ sites/\ cm^2\ of\ geometric\ area}}$$

The number of total hydrogen turnover can be calculated according to [20]:
$\left(|j|\frac{\mathrm{mA}}{\mathrm{cm}^2}\right)\left(\frac{1\mathrm{A}}{1000\mathrm{mA}}\right)\left(\frac{\frac{1C}{s}}{1\mathrm{A}}\right)\left(\frac{6.241\times10^{18}e^-}{1C}\right)\left(\frac{1\mathrm{H_2}}{2e^-}\right)=\left(3.12\times10^{15}\frac{\frac{\mathrm{H_2}}{s}}{\mathrm{cm}^2}\right)|j|$, where j is taken from the polarization curves.

In general, the HER activity of a sample is the average activity from the various sites of the sample. For samples with rough surface, the number of the active sites per unit surface is usually estimated to be the 2/3 power of the ratio of the number of Sn and Te atoms in a SnTe unit cell over the unit volume [21-23].

The number of the active sites of the SnTe (001), (111) and (211) samples per real surfaces area can be calculated using the parameters presented below:

SnTe unit cell	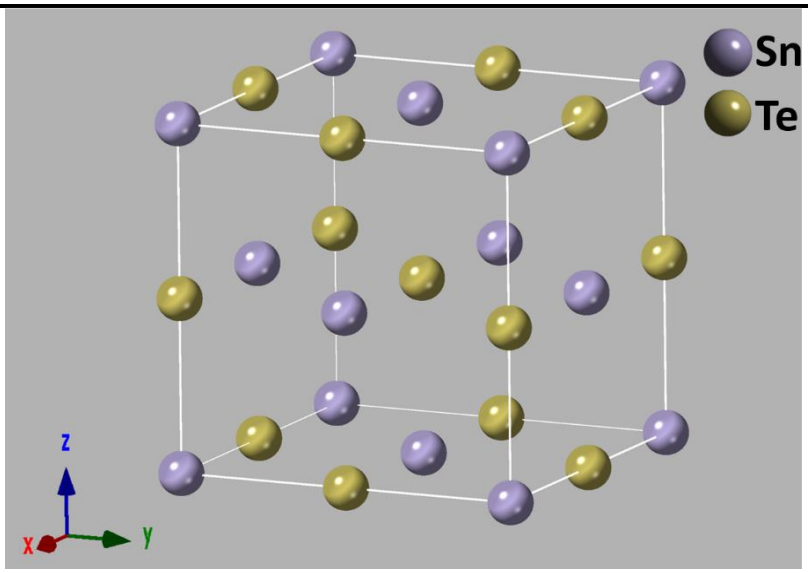
Volume	251.598 Å^3
Contains	4 Te atoms, 4 Sn atoms

$$\text{Active sites}_{\text{SnTe}}=\left(\frac{8\ \text{atoms/unit cell}}{251.598\ \text{Å}^3/\text{unit cell}}\right)^{\frac{2}{3}}=1.004\times10^{15}\ \text{atom}\ \text{cm}_{\text{real}}^{-2}$$

The TOF values of the SnTe (001), (111), and (211) samples can be calculated by the following equation:

$$\text{TOF}=\frac{3.12\times10^{15}\frac{\mathrm{H_2/s}}{\mathrm{cm}^2}}{1.004\times10^{15}\ \text{atom}\ \text{cm}_{\text{real}}^{-2}\times\text{A}_{\text{ECSA}}^{\text{SnTe}}}\ |j|.$$

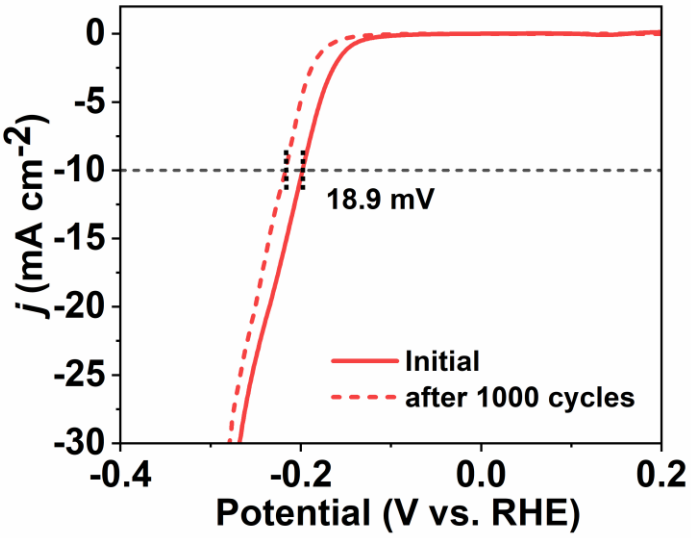

Figure S9. Polarization curves (*iR*-corrected) of the SnTe (001) sample recorded before and after 1000 cycles of cyclic voltammetry (CV) using accelerated degradation tests (scan rate = 100 mV s^{-1}).

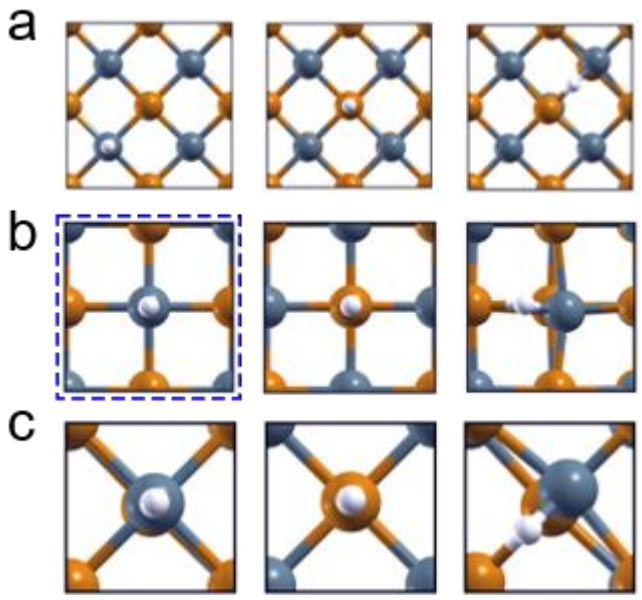

Figure S10. Top views of hydrogen adsorption on pure SnTe (001) surface at Sn, Te and Sn-Te bridge sites with hydrogen coverage of (a) 1/8 ML (b) 1/4 ML and (c) 1/2 ML. The blue dashed box highlights the most stable adsorption structure with hydrogen coverage of 1/4 ML.

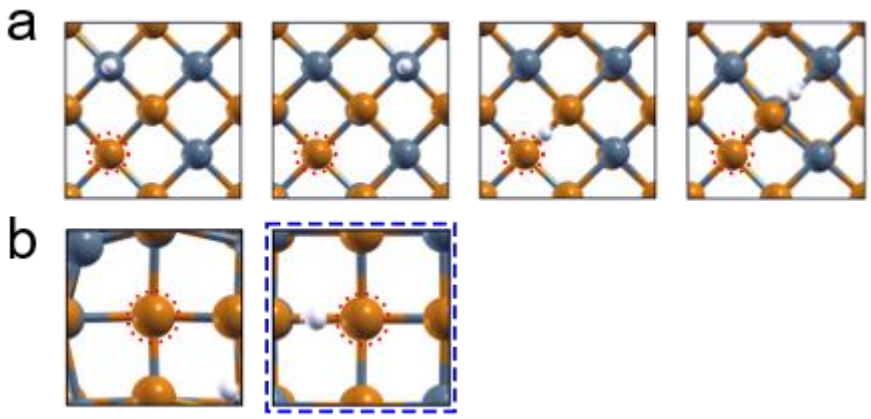

Figure S11. Top views of hydrogen adsorption on Sn-vacancy-containing SnTe (001) surface at different adsorption sites with hydrogen coverage of (a) 1/8 ML and (b) 1/4 ML. Red dashed circles indicate Sn-vacancy positions. The blue dashed box highlights the most stable adsorption structure with hydrogen coverage of 1/4 ML.

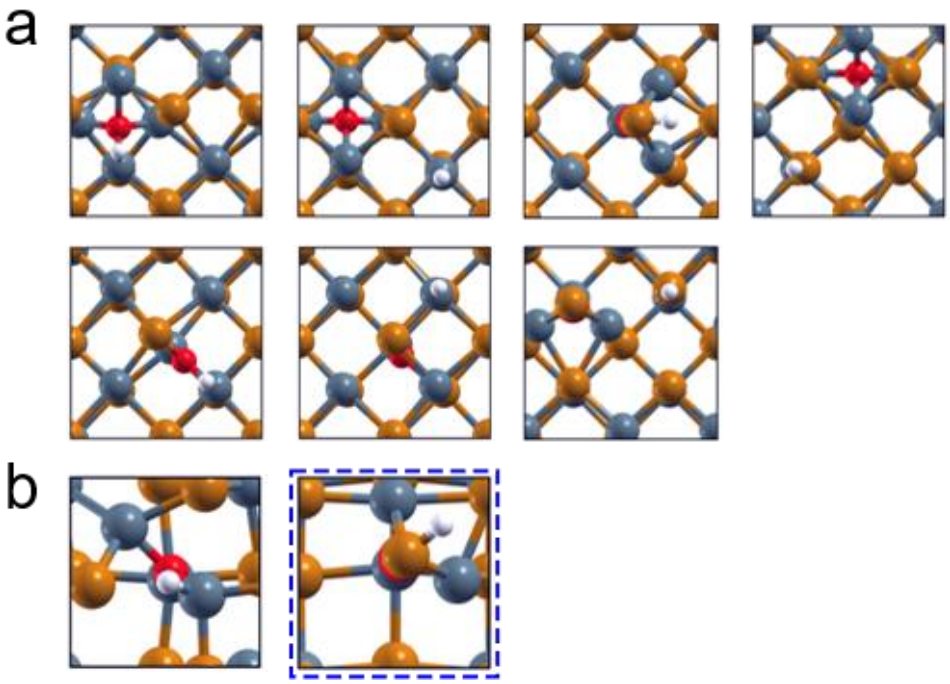

Figure S12. Top views of hydrogen adsorption on partially oxidized SnTe (001) surface at different adsorption positions with hydrogen coverage of (a) 1/8 ML and (b) 1/4 ML. The blue dashed box highlights the most stable adsorption structure with hydrogen coverage of 1/4 ML.

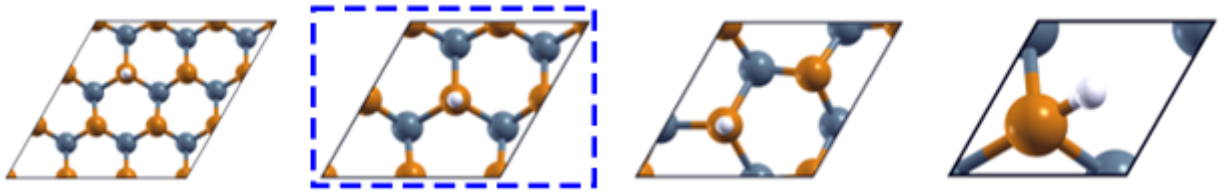

Figure S13. Top views of hydrogen adsorption on pure SnTe (111) surface with hydrogen coverage of 1/9 ML, 1/4 ML, 1/3 ML and 1 ML (from left to right). According to the surface symmetry, only one energetically stable hydrogen adsorption configuration can be obtained on each unit cell. The blue dashed box highlights the most stable adsorption structure with hydrogen coverage of 1/4 ML.

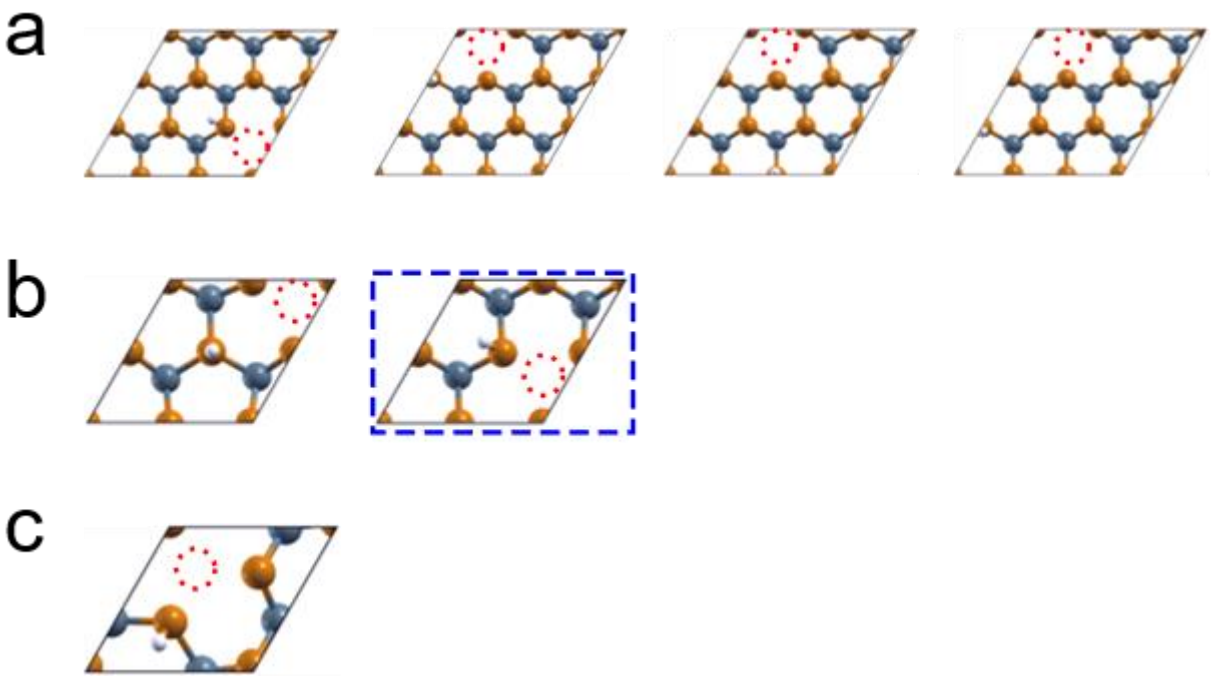

Figure S14. Top views of hydrogen adsorption on Sn-vacancy-containing SnTe (111) surface with hydrogen coverage of (a) 1/9 ML, (b) 1/4 ML and (c) 1/3 ML. Red dashed circles indicate Sn-vacancy positions. The blue dashed box highlights the most stable adsorption structure with hydrogen coverage of 1/4 ML.

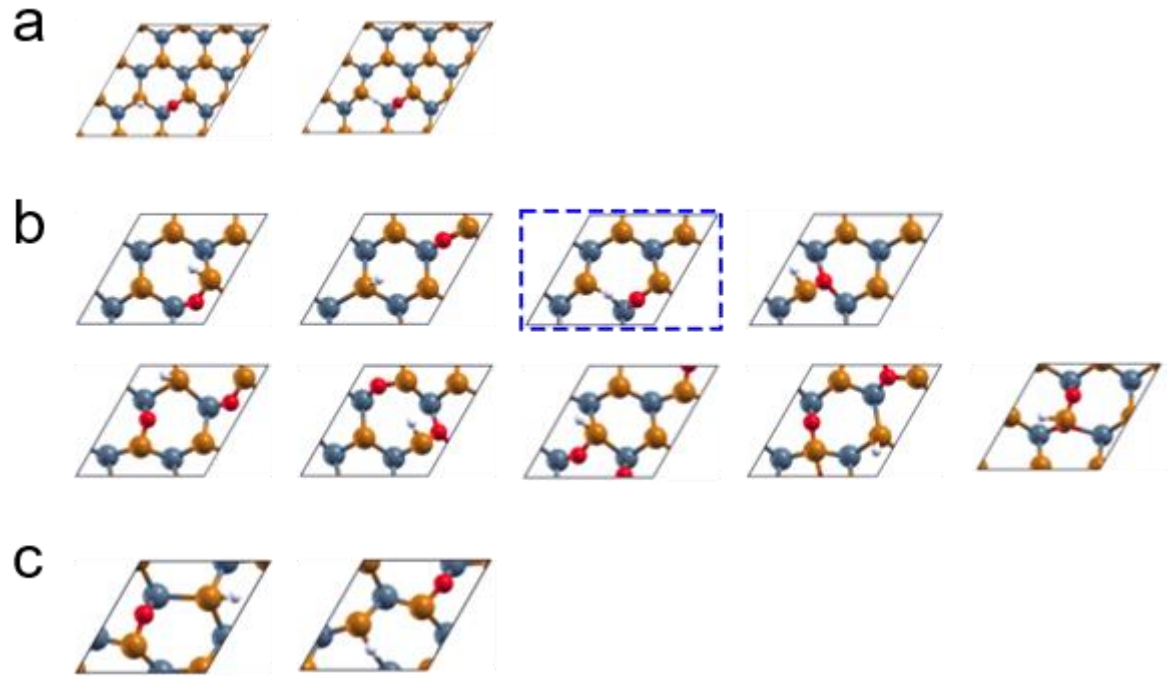

Figure S15. Top views of hydrogen adsorption on partially oxidized SnTe (111) surface at different adsorption positions with hydrogen coverage of (a) 1/9 ML, (b) 1/4 ML and (c) 1/3 ML. The upper panel of (b) includes one oxygen atom and the lower panel includes two oxygen atoms onto (111) surface. The blue dashed box highlights the most stable adsorption structure with hydrogen coverage of 1/4 ML.

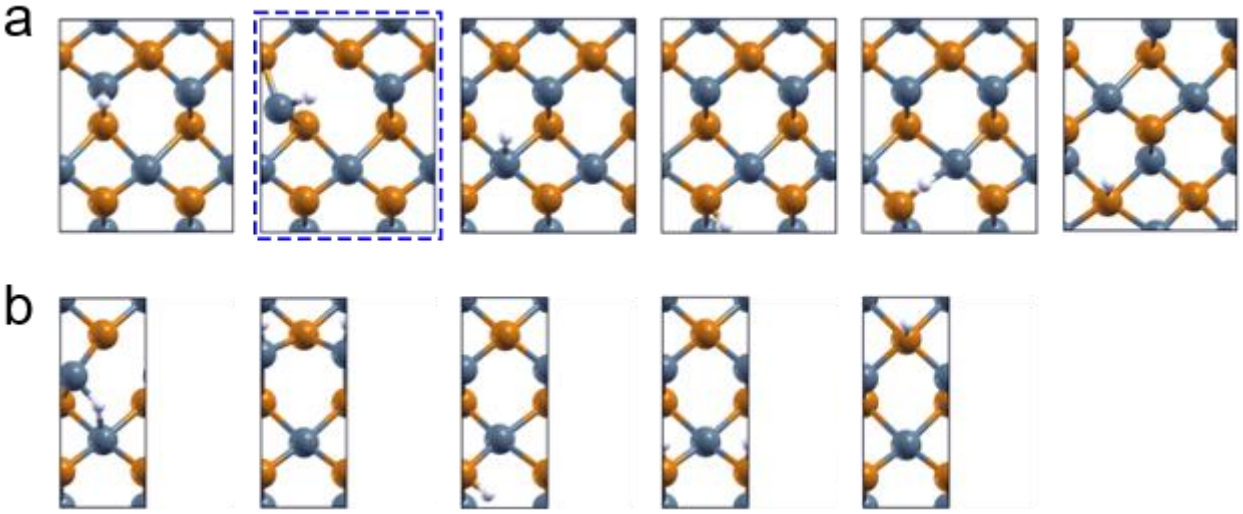

Figure S16. Top views of hydrogen adsorption on pure SnTe (211) surface at different adsorption positions with hydrogen coverage of (a) 1/4 ML and (b) 1/2 ML. The blue dashed box highlights the most stable adsorption structure with hydrogen coverage of 1/4 ML.

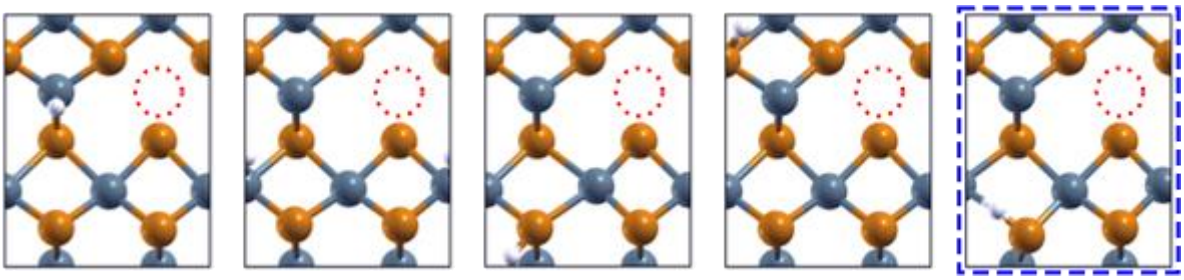

Figure S17. Top views of hydrogen adsorption on Sn-vacancy-containing SnTe (211) surface at different adsorption positions with hydrogen coverage of 1/4 ML. Red dashed circles indicate the Sn-vacancy positions. The blue dashed box highlights the most stable adsorption structure.

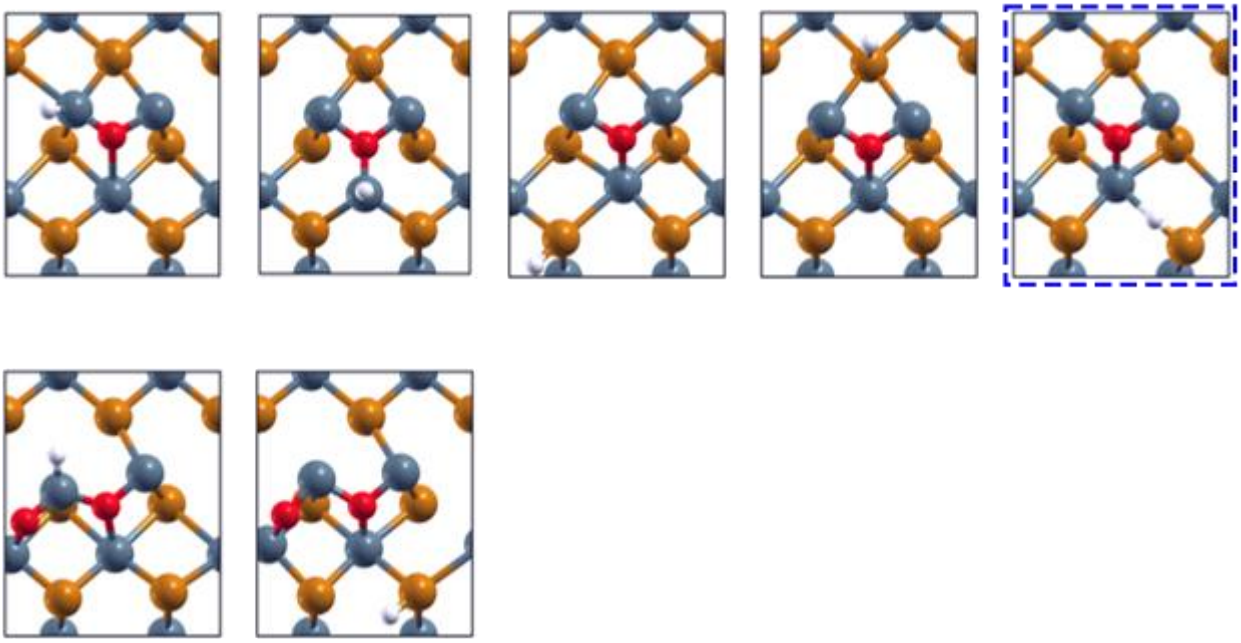

Figure S18. Top views of hydrogen adsorption on partially oxidized SnTe (211) surface at different adsorption positions with hydrogen coverage of 1/4 ML. The upper panel includes one oxygen atom and the lower panel includes two oxygen atoms onto (211) surface. The blue dashed box highlights the most stable adsorption structure.

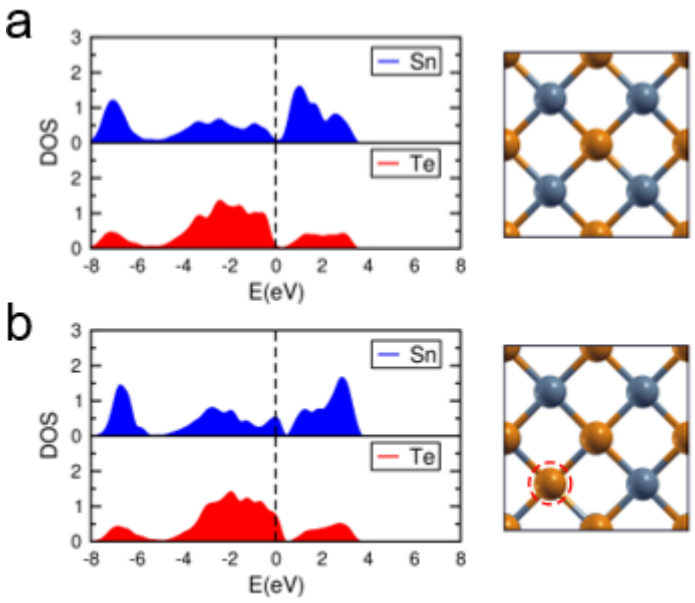

Figure S19. Projected density of states (PDOS) on the Sn (blue) and Te (red) atoms in the (a) pure and (b) Sn-vacancy-containing SnTe (001) surfaces. The right panel shows the top views of the surfaces. The red dashed circle indicates the Sn-vacancy position. Black dashed lines represent the Fermi levels.

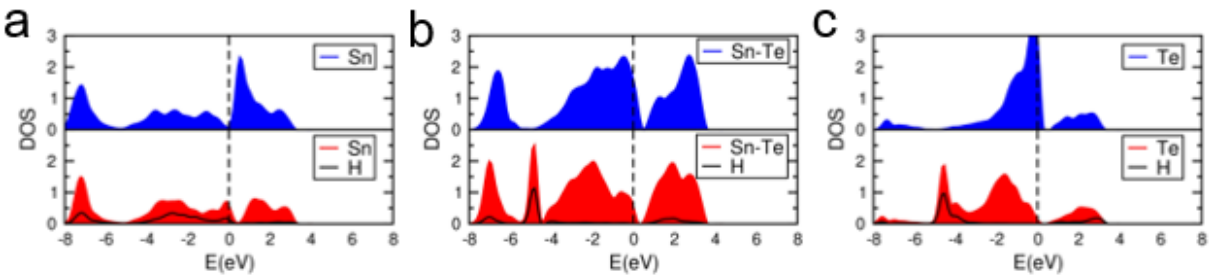

Figure S20. PDOS on hydrogen-hosting sites on (a) pure, (b) Sn-vacancy containing, and (c) partially oxidized SnTe (001) surfaces before (blue) and after (red) hydrogen adsorption. The solid black curve is the PDOS on the H atom. Black dashed lines represent the Fermi levels.

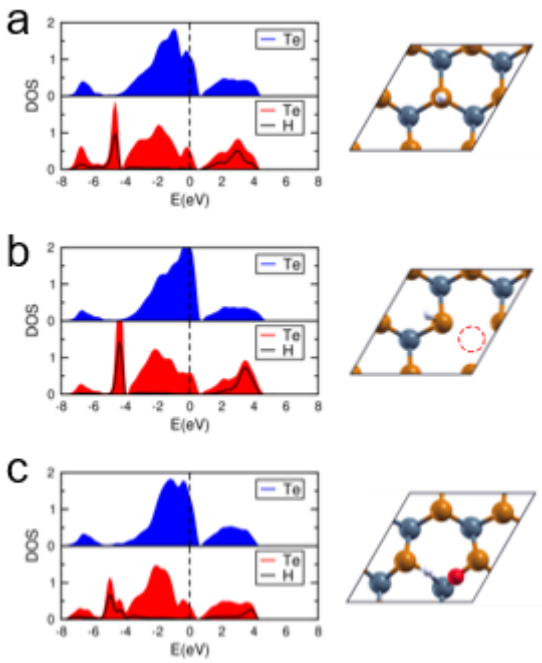

Figure S21. PDOS on the hydrogen-hosting Te atom on (a) pure, (b) Sn-vacancy-containing, and (c) partially oxidized SnTe (111) surface before (blue) and after (red) hydrogen adsorption. The right panel shows the top views of surfaces. The red dashed circle indicates the Sn-vacancy position. The solid black curve is the PDOS on the H atom. Black dashed lines represent the Fermi levels.

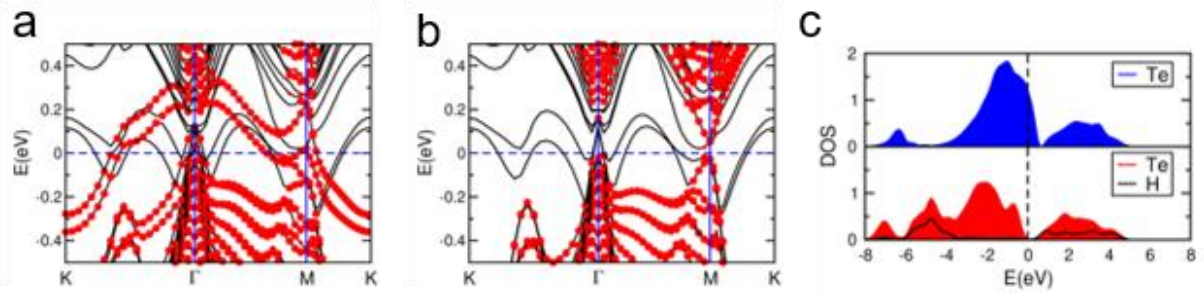

Figure S22. Band structures of (1×1) 48ML SnTe (111) slab (a) before and (b) after hydrogen adsorption. The sizes of red dots represent the contributions from (111) upper 6ML surface. (c) PDOS on Te atom before (blue) and after (red) hydrogen adsorption with 1ML coverage. The solid black curve is the PDOS on the H atom. The Fermi levels are set to zero.

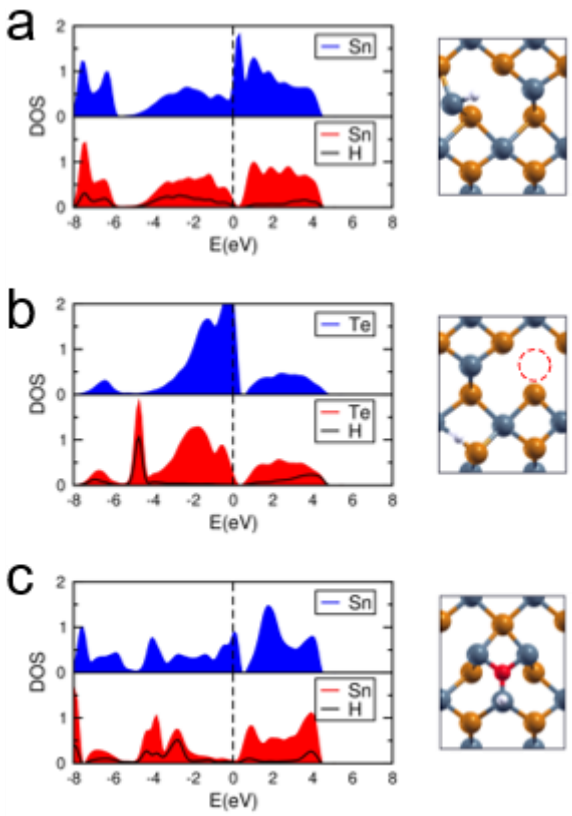

Figure S23. PDOS on the Te and Sn atoms in (a) pure and (b) Sn-vacancy-containing and (c) partially oxidized SnTe (211) surfaces before (blue) and after (red) hydrogen adsorption. The right panel shows the top views of atomic structures. The red dashed circle labels the position of a Sn vacancy. The solid black curve is the PDOS on the H atom. Black dashed lines represent the Fermi levels.

Supplementary note 2

Hydrogen adsorption on Sn-terminated (111) surface

Besides the Te-terminated (111) surfaces discussed in the main text, we also considered the HER activity of Sn-terminated (111) surfaces. As indicated by previous studies [24-26], surface reconstruction may occur on Sn-terminated (111) surfaces to cancel the internal dipole moment. Using first-principles DFT calculations, Wang et al. demonstrated that the (2×1)-1 Sn (111) surface with 50% Sn coverage could exist under a Sn-rich condition [24]. Figure S24 shows the band structure of a (2×1)-1Sn (111) slab whose thickness is 39ML. The mirror-symmetry protected Dirac cone is located near the Γ point, which has a small density of states at the Fermi level (Figure S25a). The hydrogen atom is repelled by the surface and ΔG_{H} is 0.85 eV (Figure S26).

Next we considered the effect of partial oxidation on the (2×1)-1Sn (111) surface by adding one oxygen atom onto the surface (Figure S27). The ΔG_{H} value largely decreases to 0.18 eV, indicating the high electrocatalytic activity for the HER. Electronic structure calculations

(Figure S25b) show that the Dirac cone upshifts above the Fermi level, making the slab a p-type material. The charge transfer between the H atom and the surface enables the formation of a H-Te bond, which enhances the HER performance. These results regarding the magnitude of ΔG_{H} and the location of the Dirac cone are consistent with our finding on the (001) and Te-terminated (111) surface.

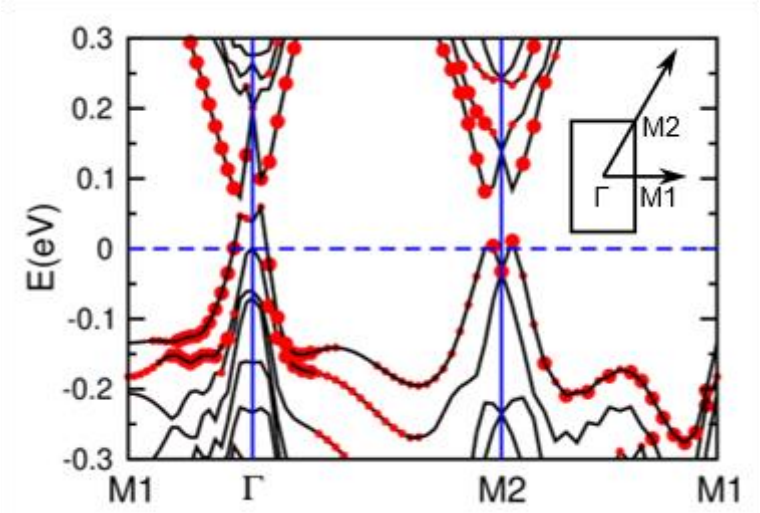

Figure S24. Band structure of pure (2×1)-1Sn (111) surface with 39 ML thickness. The size of red dots represents the contributions from the upper 6ML in the (111) surface slab. The Fermi level is set to zero.

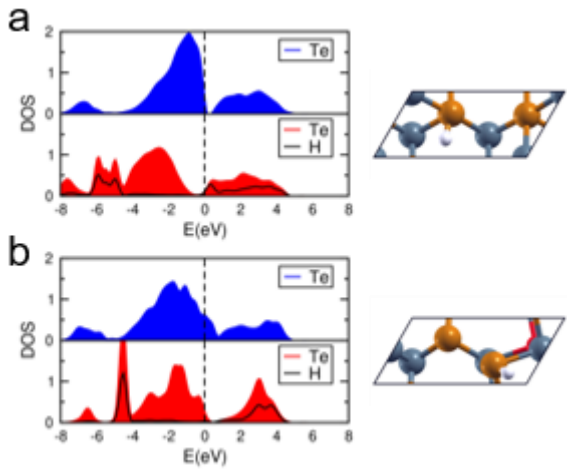

Figure S25. PDOS on hydrogen-hosting Te atom on (a) pure and (b) partially oxidized (2×1)-1Sn (111) surfaces before (blue) and after (red) hydrogen adsorption. The right panel shows the top views of the atomic structures. The solid black curve is the PDOS on the H atom. Black dashed lines represent the Fermi levels.

Figure S26. Top views of hydrogen adsorption on (2×1)-1Sn (111) surface at different adsorption sites.

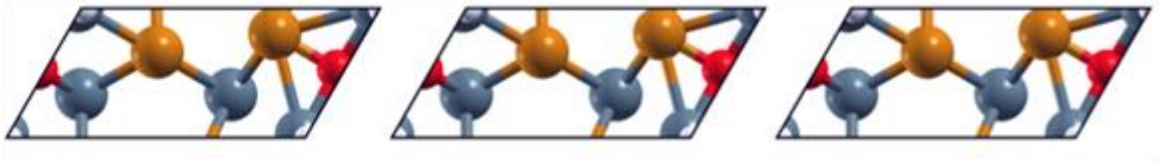

Figure S27. Top views of hydrogen adsorption on partially oxidized (2×1)-1Sn (111) surface at different adsorption sites.

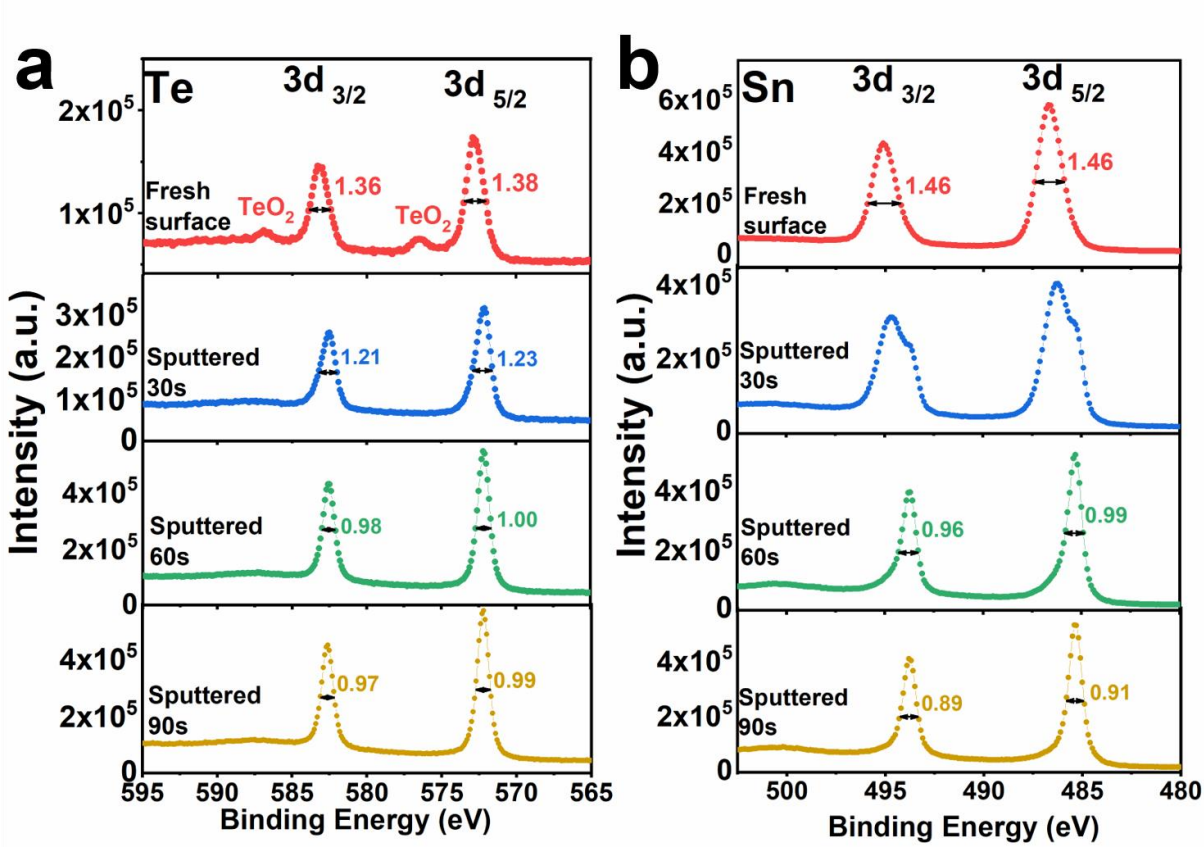

Figure S28. Raw data of Te 3d (a) and Sn 3d (b) XPS spectra of the SnTe (001) sample for its fresh surface, and those after sputtering for 30s, 60s, and 90s.

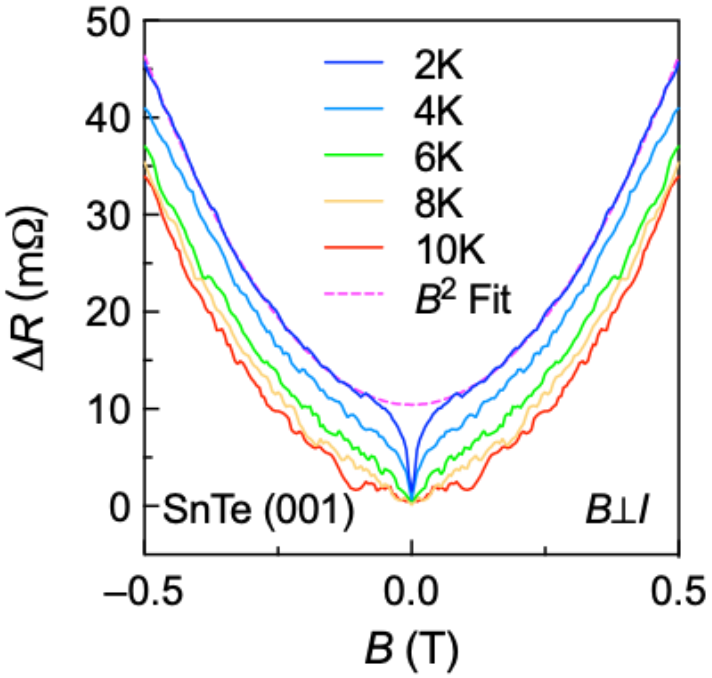

Figure S29. Magnetoresistance (ΔR=R(B)-R(0)) in SnTe (001) under out-of-plane magnetic field at different temperatures. The purple dash line is the classic parabolic magnetoresistance fitted based on high field data.

Supplementary note 3

Theoretical Calculations

For hydrogen adsorption simulations, we used (1×1), $c(2 \times 2)$, and (2×2) unit cells of SnTe (001) with 8ML thick; (1×1), $(\sqrt{3} \times \sqrt{3})$R30°, (2×2) and (3×3) unit cells of Te-terminated (111) with 10ML thick; (2×1)-1Sn (111) with 10ML thick; (1×1) and (2×1) unit cells of SnTe (211) with 15ML thick. For electronic structure calculations, we used a 12ML SnTe (001) slab, a 24ML Te-terminated SnTe (111) slab, a 39ML (2×1)-1Sn (111) slab, and a 24ML SnTe (211) slab. We used a $6 \times 6 \times 1$ Monkhorst-Pack k-point mesh for the structural optimization of the (1×1) SnTe (001) and (111) unit cells, and a $8 \times 8 \times 1$ k-point mesh for electronic structure calculations. We used a $6 \times 2 \times 1$ k-point mesh for the structural optimization of a (1×1) SnTe (211) unit cell and a $8 \times 4 \times 1$ k-point mesh for electronic structure calculations.

We calculated ΔG_{H} as:

$$\Delta G_{\mathrm{H}} = \Delta E_{\mathrm{H}} + \Delta E_{\mathrm{ZPE}} - T\Delta S_{\mathrm{H}} \quad (1)$$

ΔE_H denotes the hydrogen absorption energy calculated by:

$$\Delta E_{\mathrm{H}} = E\left[\mathrm{SnTe} + \mathrm{H}^{\mathrm{ad}}\right] - E[\mathrm{SnTe}] - \frac{1}{2}E[\mathrm{H_2}] \quad (2)$$

where $E[\mathrm{SnTe} + \mathrm{H^{ad}}]$ is the total energy of the SnTe slab adsorbed by a H atom, $E[\mathrm{SnTe}]$ is the energy of the SnTe slab after removing the H atom, and $E[\mathrm{H_2}]$ is the energy of a hydrogen molecule in the gas phase. We calculated the zero-point energy change of a H atom, ΔE_{ZPE}, as

$$\Delta E_{\mathrm{ZPE}} = E_{\mathrm{ZPE}}[\mathrm{H^{ad}}] - \frac{1}{2}E_{\mathrm{ZPE}}[\mathrm{H_2}] \quad (3)$$

where $E_{\mathrm{ZPE}}[\mathrm{H^{ad}}]$ is the zero-point energy of the H atom adsorbed on the SnTe surface, and $E_{\mathrm{ZPE}}[\mathrm{H_2}]$ is the zero-point energy of a hydrogen molecule in the gas phase. ΔS_{H} is calculated as $-\frac{1}{2}S^0_{\mathrm{H_2}}$, where $S^0_{\mathrm{H_2}}$ is the entropy of H_2 in the gas phase at the standard condition (130.68 $\mathrm{J \cdot mol^{-1} \cdot K^{-1}}$ at $T = 298$ K and $p = 1$ bar)[27]. After substituting the last two terms into equation (3), we have $\Delta G_{\mathrm{H}} = \Delta E_{\mathrm{H}} + 0.25$ eV.

Table S1. Composition of the Bi_2Te_3:Fe layer of the SnTe (111) sample determined by EDS.

Layer	Bi	Te	Fe
Bi_2Te_3:Fe	41.1%	58.1%	0.8%

Table S2. Free energies of hydrogen adsorption (ΔG_{H}) on a Sn atom, a Te atom, and a Sn-Te bridge on pure and Sn-vacancy-containing surfaces of a (2×2) SnTe (001) slab.

	$\Delta G_{\mathrm{H}}(eV)$	
active site	Pure	Sn-vacancy-containing
Sn atom	0.627	0.374
Te atom	1.138	0.43
Sn-Te bridge	1.139	0.304

Table S3. Löwdin charges of the hydrogen atom adsorbed on pure, Sn-vacancy-containing, and partially oxidized surfaces of SnTe (001), (111), and (211) slabs.

Löwdin Charge on Hydrogen			
surface	(001)	(111)	(211)
pure	1.1295	0.9903	1.1206
Sn-vac	1.0475	0.988	1.0445
Oxi	0.9962	0.9839	1.1136

References

[1] Qu, Q.; Liu, B.; Liang, J.; Li, H.; Wang, J.; Pan, D.; Sou, I. K. Expediting Hydrogen Evolution through Topological Surface States on Bi_2Te_3. *ACS Catalysis* **2020,** *10*, 2656-2666.

[2] Kim, K.-C.; Lee, J.; Kim, B. K.; Choi, W. Y.; Chang, H. J.; Won, S. O.; Kwon, B.; Kim, S. K.; Hyun, D.-B.; Kim, H. J.; Koo, H. C.; Choi, J.-H.; Kim, D.-I.; Kim, J.-S.; Baek, S.-H. Free-electron creation at the 60° twin boundary in Bi_2Te_3. *Nature Communications* **2016,** *7*, 12449.

[3] Liang, J.; Zhang, Y. J.; Yao, X.; Li, H.; Li, Z.-X.; Wang, J.; Chen, Y.; Sou, I. K. Studies on the origin of the interfacial superconductivity of $Sb_2Te_3/Fe_{1+y}Te$ heterostructures. *Proceedings of the National Academy of Sciences* **2020,** *117*, 221.

[4] Wang, X. J.; Hou, Y. B.; Chang, Y.; Becker, C. R.; Klie, R. F.; Sivananthan, S. Microstructure of Heteroepitaxial ZnTe Grown on GaAs(211)B by Molecular Beam Epitaxy. *Journal of Electronic Materials* **2009,** *38*, 1776-1780.

[5] Wang, X. J.; Chang, Y.; Becker, C. R.; Grein, C. H.; Sivananthan, S.; Kodama, R. Microstructure of Heteroepitaxial ZnTe Grown by Molecular Beam Epitaxy on Si(211) Substrates. *Journal of Electronic Materials* **2011,** *40*, 1860-1866.

[6] A. Smith, J. F. Baumard, P. Abélard, M. F. Denanot, *J. Appl. Phys.* **1989**, *65*, 5119.

[7] J. R. Macdonald, *Impedance spectroscopy : emphasizing solid materials and systems*, Wiley, New York, **1987**.

[8] C. P. Lindsey, G. D. Patterson, *J. Chem. Phys.* **1980**, *73*, 3348.

[9] A. K. Jonscher, *Phys. Status Solidi A* **1975**, *32*, 665.

[10] J. L. Gilbert, Electrochemical behavior of metals in the biological milieu. In *Comprehensive Biomaterials, Vol. 1*, Elsevier, **2011**, pp. 21.

[11] R. de Levie, *J. Electroanal. Chem. Interf. Electrochem.* **1989**, *261*, 1.

[12] A. Popova, S. Raicheva, E. Sokolova, M. Christov, *Langmuir* **1996**, *12*, 2083.

[13] L. Nyikos, T. Pajkossy, *Electrochim. Acta* **1990**, *35*, 1567.

[14] W. H. Mulder, J. H. Sluyters, T. Pajkossy, L. Nyikos, *J. Electroanal. Chem. Interf. Electrochem.* **1990**, *285*, 103.

[15] B.-A. Mei, J. Lau, T. Lin, S. H. Tolbert, B. S. Dunn, L. Pilon, *J. Phys. Chem. C* **2018**, *122*, 24499.

[16] D. C. Grahame, *Chem. Rev.* **1947**, *41*, 441.

[17] R. Kötz, M. Carlen, *Electrochim. Acta* **2000**, *45*, 2483.

[18] B. E. Conway, B. V. Tilak, *Electrochim. Acta* **2002**, *47*, 3571.

[19] J. D. Benck, Z. Chen, L. Y. Kuritzky, A. J. Forman, T. F. Jaramillo, *ACS Catal.* **2012**, *2*, 1916.

[20] Z. Chen, D. Cummins, B. N. Reinecke, E. Clark, M. K. Sunkara, T. F. Jaramillo, *Nano Lett.* **2011**, *11*, 4168.

[21] X.-D. Wang, Y.-F. Xu, H.-S. Rao, W.-J. Xu, H.-Y. Chen, W.-X. Zhang, D.-B. Kuang, C.-Y. Su, *Energ & Environ. Sci.* **2016**, *9*, 1468.

[22] J. Kibsgaard, T. F. Jaramillo, *Angew Chem. Int. Edit.* **2014**, *53*, 14433.

[23] R. Zhang, X. Wang, S. Yu, T. Wen, X. Zhu, F. Yang, X. Sun, X. Wang, W. Hu, *Adv. Mater.* **2017**, *29*, 1605502.

[24] J. Wang, J. Liu, Y. Xu, J. Wu, B.-L. Gu, W. Duan, *Phys. Rev. B* **2014**, *89*, 125308.

[25] V. L. Deringer, R. Dronskowski, *ChemPhysChem* **2013**, *14*, 3108.
[26] F. Finocchi, A. Barbier, J. Jupille, C. Noguera, *Phys. Rev. Lett.* **2004**, *92*, 136101.
[27] P. Atkins, J. De Paula, *Atkins' Physical chemistry*, Oxford university press, Oxford, **2006**.